J. Fluid Mech. (2013), *vol.* 728, *pp.* 362–375. © Cambridge University Press 2013
doi:10.1017/jfm.2013.271

Direct numerical evidence of stress-induced cavitation

G. Falcucci[1,†], E. Jannelli[1], S. Ubertini[2] and S. Succi[3]

[1]Department of Technologies, University of Naples 'Parthenope', Centro Direzionale - Isola C4, 80143 Naples, Italy

[2]DEIM - Industrial Engineering School, University of Tuscia, Largo dell'Universitá s.n.c., 01100, Viterbo, Italy

[3]Istituto Applicazioni Calcolo, CNR, Via dei Taurini 19, 00185 Rome, Italy

(Received 7 December 2012; revised 12 March 2013; accepted 23 May 2013; first published online 11 July 2013)

In this paper direct numerical evidence of flow-induced incipient cavitation is presented through lattice Boltzmann simulations of multiphase flows with a non-ideal thermodynamic equation of state. Cavitation emerges spontaneously as a result of the underlying non-ideal interactions, with no need for any modelling criteria based on the fluid variables, such as pressure or stress tensor. The onset of cavitation is well captured by Joseph's minimum tension criteria, (Joseph, *J. Fluid Mech.*, vol. 366, 1998, pp. 367–378; Dabiri, Sirignano & Joseph, *Phys. Fluids*, vol. 19, 2007, 072112), complemented with surface tension corrections, as proposed by Brennen (*Cavitation and Bubble Dynamics*, Oxford University Press, 1995). The simulations also show that the cavitation number (C_N) proves to be a poor predictor of the onset of cavitation. Finally, strong dependence of the bubble morphology on the surface tension is also highlighted.

Key words: cavitation, computational methods, multiphase flow

1. Introduction

Cavitation is a major fluid-dynamic phenomenon, characterized by the formation of liquid-free regions (bubbles or cavities) where static pressure drops below a certain threshold, due to abrupt mechanical changes in the flow configuration, i.e. fluid flowing through thin orifices, or experiencing sudden changes of direction. It may be an aggressive phenomenon, hence a major concern for many engineering applications dealing with materials in contact with high-speed flows, such as turbines and propellers (Brennen 1995; Kumar & Saini 2010). This aggressiveness is due to its capability to focus substantial amounts of fluid energy within narrow regions of space (the bubbles), which subsequently release this energy back in the form of violent implosions and resulting emission of shock and light waves (Hilgenfeldt *et al.* 1998; Bremond *et al.* 2005; Lohse 2005; Ohl *et al.* 2006). The shock waves formed by cavitation are sufficiently strong to significantly damage moving parts and, consequently, minimizing cavitation, especially in the proximity of critical structures, is a major concern in the design of fluid machinery and hydraulic machines in

† Email address for correspondence: giacomo.falcucci@uniparthenope.it

https://doi.org/10.1017/jfm.2013.271 Published online by Cambridge University Press

general. Moreover, the occurrence of cavitation in orifices and nozzles has a significant influence on the atomization of the exiting liquid jet, making it a fundamental topic in spray dynamics. Since cavitation can be regarded as a strongly off-equilibrium non-thermal phase transition, the subject is also of interest for fundamental studies of non-equilibrium thermodynamics (Brennen 1995; Franc & Michel 2005; Zwaan *et al.* 2007).

Cavitating phenomena are highly sensitive to local interface dynamics. The response of cavitating flows to external perturbations, for instance a sudden drop in the local pressure, differs significantly from the case of standard multiphase flows, due to the non-thermal nature of the bubble formation process. Cavitating flows are subject to rapid changes (with respect to typical hydrodynamic scales) in the local pressure distribution, which may trigger potential instabilities, such as growth in surface oscillations, eventually leading to bubble collapse (implosion) and/or interface rupture.

It is challenging to capture direct experimental evidence of the morphology of real-scale cavitating flows, due to the transient dynamics at very short spatial scales and to the practical difficulty of using non-intrusive probes. Indeed, the presence of a cavitation region is typically inferred *ex post*, i.e. by measuring and detecting its effects, such as spray formation and aspect, vibrations and acoustic emissions (Pecha & Gompf 2000; Brujan, Ikeda & Matsumoto 2012).

It is possible to visualize the light reflected by the interface using transparent liquids (Giannadakis *et al.* 2007). However, such a technique can only be used in much larger nozzles than the real-scale injectors, with very significant scale effects (Payri *et al.* 2012).

Cavitating flows set a challenge also for numerical simulations. The difficulties in numerical simulations of cavitating flows for solvers based on Navier–Stokes (NS) equations are related to the dynamic tracking of the interface between the two fluids. Different cavitation models are available in literature, such as the cavitation bubble-tracking model of Gavaises *et al.* (2007), but cavitation is also studied by means of advanced single-phase approaches (Lee & Reitz 2009).

Generally such models augment the NS equations with a surface-tension force acting upon the unknown interface. The interface itself is located by means of semi-empirical criteria based on the space–time distribution of the pressure or other thermodynamic fields, a methodology that one may call ‘cavitation modelling’ (Zaleski, Li & Succi 1995; Joseph 1998; Dabiri, Sirignano & Joseph 2007; Giannadakis *et al.* 2007). Within the LB approach, no such modelling is needed, because the liquid–gas interface emerges spontaneously from of the underlying intermolecular interactions, as encoded within the corresponding non-ideal equation of state (EOS) and surface tension. The lattice Boltzmann (LB) method has been used with success for a wide body of multiphase and multicomponent flow applications, but its viability for cavitation studies has been addressed only very recently (Sukop & Or 2005; Darbandi & Sadeghi 2010; Chen, Zhong & Yuan 2011; Zhong, Zhong & Bai 2012; Falcucci *et al.* 2013).

In this work, we find that Joseph’s minimum tension criterion (Joseph 1998; Dabiri *et al.* 2007) correctly captures the onset of incipient cavitation, provided the cavitation threshold is corrected by means of surface-tension terms, as proposed by Brennen (1995, §§ 1.7 and 1.13), based on the seminal work by Epstein & Plesset (1950) and Plesset & Prosperetti (1977).

Different non-dimensional cavitation numbers are considered and the effects of surface tension on the dynamic morphology of the cavitating bubbles are also explored.

https://doi.org/10.1017/jfm.2013.271 Published online by Cambridge University Press

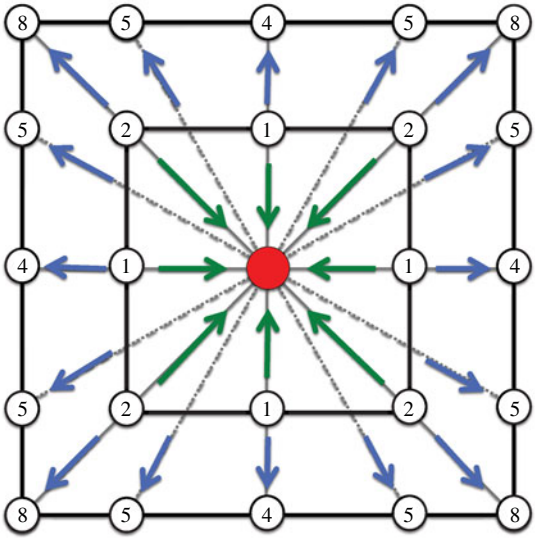


FIGURE 1. (Colour online) Sketch of the forces acting on the Brillouin zones of the two-belt approach: the attractive force $\boldsymbol{F}_1(\boldsymbol{x}, t)$ acts on the first belt, composed of $b_1 = 8$ neighbours; the repulsive force $\boldsymbol{F}_2(\boldsymbol{x}, t)$ acts on both belts, with $b_2 = 24$ neighbours.

2. LB for non-ideal fluids: the two-belt approach

The LB method is a numerical technique to study fluid dynamics, based on a minimal form of (lattice) Boltzmann's kinetic equation. It is characterized by a statistical discrete approach rather than by the continuum assumption underlying all numerical solvers based on NS equations (Succi 2001). The LB method has been successfully employed recently in the field of multiphase flows (Shan & Chen 1993, 1994; Falcucci *et al.* 2007; Sbragaglia *et al.* 2007; Falcucci *et al.* 2010*a*; Falcucci, Ubertini & Succi 2010*b*; Falcucci *et al.* 2011; Colosqui *et al.* 2012; Falcucci *et al.* 2013), proving a robust and efficient alternative to the NS approach.

The standard LB equation with pseudo-potential interaction reads as follows (with unit time step for simplicity):

$$f_i(\boldsymbol{x} + \boldsymbol{c}_i, t + 1) - f_i(\boldsymbol{x}, t) = -\omega(f_i - f_i^{eq}) + F_i(\boldsymbol{x}), \tag{2.1}$$

where f_i is the probability density function of finding a particle at site $\boldsymbol{x}$ at time t, moving along the ith lattice direction defined by the discrete speeds $\boldsymbol{c}_i$ with $i = 0, \ldots, b$. The left hand-side of (2.1) stands for molecular free streaming, whereas the right-hand side represents the time relaxation (due to collisions) towards local Maxwellian equilibrium.

Finally, F_i represents the bias on the ith population due to the volumetric force $\boldsymbol{F}(\boldsymbol{x}, t)$. This is represented by the sum of the two forces proposed by Falcucci *et al.* (2007) (see figure 1), $\boldsymbol{F}(\boldsymbol{x}, t) = \boldsymbol{F}_1(\boldsymbol{x}, t) + \boldsymbol{F}_2(\boldsymbol{x}, t)$, with $\boldsymbol{F}_1(\boldsymbol{x}, t) = G_1\psi(\boldsymbol{x}, t)\sum_{i=0}^{b_1} w_{i,1}\psi(\boldsymbol{x} + \boldsymbol{c}_{i,1}, t)\boldsymbol{c}_{i,1}$ acting on the first belt of neighbours and $\boldsymbol{F}_2(\boldsymbol{x}, t) = G_2\psi(\boldsymbol{x}, t)\sum_{i=0}^{b_1} w_{i,1}\psi(\boldsymbol{x} + \boldsymbol{c}_{i,1}, t)\boldsymbol{c}_{i,1} + G_2\psi(\boldsymbol{x}, t)\sum_{i=0}^{b_2} w_{i,2}\psi(\boldsymbol{x} + \boldsymbol{c}_{i,2}, t)\boldsymbol{c}_{i,2}$ acting on both belts (Falcucci *et al.* 2007). The coupling parameters G_1 and G_2 have been chosen, according to our previous works, in such a way as to realize a density jump between the phases of $\sim$1:30.

https://doi.org/10.1017/jfm.2013.271 Published online by Cambridge University Press

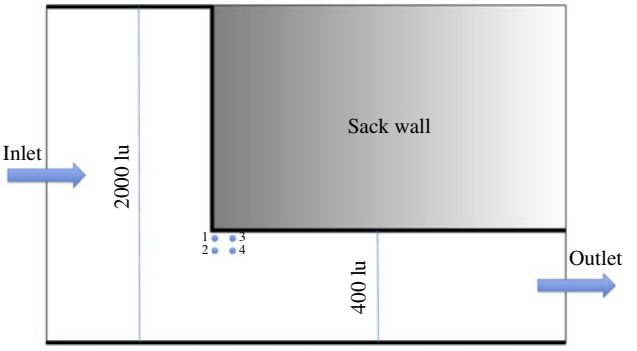


FIGURE 2. (Colour online) Sketch of the computational domain. The solid line represents a non-slip wall boundary condition. The presence of the four probes, used to monitor pressure and kinetic energy inside the cavitation region, is also highlighted.

The resulting EOS reads as $P = \rho c_s^2 + ((G_1 + G_2)c_s^2[\psi(\rho)]^2)/2$, with $\psi(\rho) = \rho_0(1 - \mathrm{e}^{-\rho/\rho_0})$, being $\rho_0 = 1$ for convenience. Such an EOS can be shown to support a liquid–vapour phase transition at the critical values, $\rho_{cr} = \ln 2$ and $P_{cr} = (\ln 2 - (1/2))/3$ for $G < G_{cr} = -4.0$, all in lattice units. In the above, the subscript cr indicates the critical point in the phase diagram. To be noted that the non-ideal part of the *SC* EOS depends on one single parameter because the model is purely attractive ($G < 0$). However, due to the density dependence of $\psi(\rho)$, this EOS can generate coexistence between the liquid and vapour phases. The critical density ρ_{cr} and the critical coupling strength G_{cr} are computed based on the usual requirement $\partial p/\partial\rho = 0$ and $\partial p^2/\partial^2\rho = 0$. The former delivers $\rho_{cr} = \ln 2$ and inserting this in the latter, we obtain $G_{cr} = -4.0$, from which the critical pressure follows directly from the EOS. From this discussion, we see that G_{cr} plays the role of an effective critical temperature, in the sense that for $G < G_{cr}$ the EOS shows a Van-der-Waals-like loop.

The macroscopic density ρ and velocity $\boldsymbol{u}$ are given by (Benzi, Succi & Vergassola 1992; Succi 2001), $\rho(\boldsymbol{x}, t) = \sum_{i=0}^{b} f_i$ and $\rho(\boldsymbol{x}, t)\boldsymbol{u}(\boldsymbol{x}, t) = \sum_{i=0}^{b} \boldsymbol{c}_i f_i$.

The conversion from LB to physical units proceeds as follows.

(i) Length: $L_{phys} = L_{lb}\Delta x$, where L_{phys} is the physical length (metres), Δx is the lattice spacing in physical units and L_{lb} is the length in non-dimensional (lattice) units.

(i) Time units are fixed based on $t_{phys} = t_{lb}\Delta t$, where Δt is the time step in physical units (seconds) and it is computed based on the viscosity relation, $\nu_{phys} = \nu_{lb}\Delta x^2/\Delta t$.

(i) Finally, the mass unit are such that the LB critical density, $\rho_{cr} = \ln 2$ corresponds to the critical density of the fluid under investigation.

3. Simulations, results and discussion

In this section we present a series of simulations of a multiphase fluid flowing through an orifice of height $h = 400$ lattice points (see figure 2). A constant density and velocity profile are imposed at the inlet, while at the outlet a free-flow condition and constant density are imposed. As a reference condition, we have taken the total pressure, represented by the sum of the inlet pressure and kinetic energy at the inlet section. More specifically, the inlet fluid speed u_{in} is changed in order to scan different

https://doi.org/10.1017/jfm.2013.271 Published online by Cambridge University Press

ρ_L	ρ_V	ρ_L/ρ_V	
1.9	0.068	27.94	
G_1	G_2	P_L^*	σ
−5.0	0.0	−0.602	0.0565
−10	5.0	−0.602	0.0482
−15	10.0	−0.602	0.0412

TABLE 1. Main thermodynamic characteristics of the simulations. The parameters G_1 and G_2 represent the strength of non-ideal interactions in the first and second shell of lattice neighbours, respectively and P_L^* is the corresponding excess pressure in the liquid phase at coexistence.

values of the cavitation number (C_N), defined as (Brennen 1995, § 1.13):

$$C_N = \frac{P_{in} + \rho_{in} u_{in}^2/2 - P_V}{\rho_{in} u_{in}^2/2}, \tag{3.1}$$

where P_{in} is the pressure at the inlet (reference) section, P_V the pressure in the vapour phase measured by the four probes described in figure 2 and u_{in} the reference velocity at the inlet section.

The corresponding Reynolds and Weber numbers, given by $Re = u_{in}h/\nu$ and $We = \rho_v u_{in}^2 h/\sigma$, range from $48 \leqslant Re \leqslant 600$ and $0.14 \leqslant We \leqslant 22.2$, respectively.

Cavitation is expected whenever C_N is higher than a critical value, around $C_{N,cr} \sim 1.75$ for orifices (Koivula 2000). As discussed in the introduction, the occurrence of such condition is entirely dictated by the spontaneous dynamics of the multiphase flow, with no need for any modelling criterion (Zaleski *et al.* 1995; Giannadakis, Gavaises & Arcoumanis 2008). The time evolution of the total pressure, $P = \rho c_s^2 + (G c_s^2 \psi^2(\rho))/2$, and kinetic energy, $E_k = \rho(u^2/2)$, contributions are evaluated at the four probes sketched in figure 2. The position of the probes is chosen sufficiently far from the boundaries, in order to minimize finite-size effects.

All simulations have been performed on a 1000×1000 and 2000×2000 two-dimensional domain, showing no appreciable difference between the two. For the sake of compactness, only the results of the 2000×2000 simulations are reported hereafter.

Our simulations have been performed using the multirange (two belts of neighbours) version of the Shan–Chen potential (see Appendix), with $\rho_L = 1.9$ and $\rho_V = 0.068$ corresponding to a density ratio of ∼1:30 between the vapour and liquid phase, which is typical of many applications in fluid machinery. The main parameters are reported in the table 1, in which the excess pressure is given by $P^* = (G_1 + G_2)\psi^2(\rho)c_s^2/2$.

Table 2 shows the different parameters adopted for the simulations with $G_1 = -15.0$ and $G_2 = 10.0$; t_{circ} represents the circulation time, given by $t_{circ} = L/u_{in}$ with L the domain length (i.e. 2000 in lattice units).

Figure 3 reports the pressure evolution in time, according to the four probes in figure 2, for different inlet velocities.

Table 2 summarizes the thermodynamic conditions of cavitating flows in the different configurations. Some considerations are in order.

First, with regard to the computed C_N for the different inlet velocities and corresponding to the channel height $h = 400$, table 2 shows a decrease in C_N at increasing inlet velocities. Figure 4 reports the profiles of velocity magnitude in the inlet section of the nozzle channel, normalized to the inlet value of each respective case in table 2. The highest inlet velocities associate with the lowest velocity in the

https://doi.org/10.1017/jfm.2013.271 Published online by Cambridge University Press

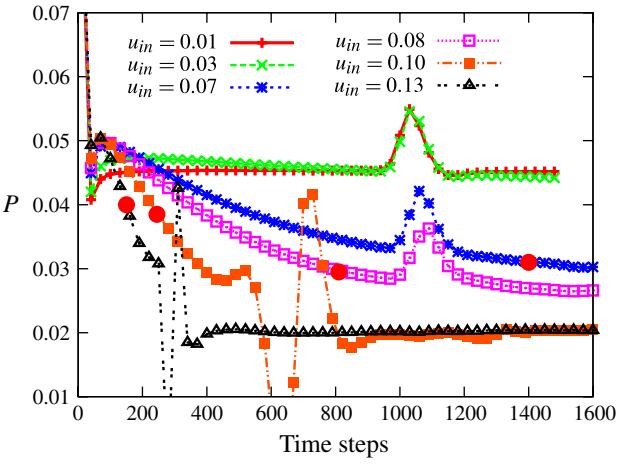


FIGURE 3. (Colour online) Pressure evolution in time for the different inlet velocities; the trends are computed according to the four probes in figure 2. The circles (shown in red online) represent the beginning of cavitation, referred to as t_{cav}. Note that t_{cav} increases as u_{in} goes down and eventually $t_{cav} \to \infty$ below a given velocity, approximately $u_{in} \sim 0.03$.

u_{in}	Re	We	$P_{in} + \frac{\rho u^2}{2}$	P_V	C_N	$t_{cav} \times 10^{-3}$	t_{cav}/t_{circ}
0.01	48	0.132	0.0438	—	—	—	—
0.03	144	1.188	0.0446	—	—	—	—
0.07	336	6.468	0.0486	0.031	3.59	1.40	0.049
0.08	384	8.450	0.0501	0.030	3.14	0.80	0.032
0.10	480	13.204	0.0537	0.039	1.47	0.25	0.012
0.13	624	22.320	0.0606	0.040	1.22	0.15	0.0097

TABLE 2. Cavitation time as a function of the inlet conditions. The dashes indicate that no cavitation has been observed within the simulation time, up to 60 000 time steps.

inlet section of the sack, an effect that we ascribe to enhanced dissipation. This is also the reason why C_N is lower in the case of high inlet velocity.

The present simulations are expected to show at least a qualitative similarity with potential flows through orifices in a plane wall. To investigate this point, we have performed further simulations and compared with previous results on potential flow through an axisymmetric orifice (Dabiri *et al.* 2007). In figure 5, we report the velocity vector field at various sections along the channel, at $Re \sim 2000$ and $t \sim 500$. Visual inspection reveals indeed a satisfactory qualitative agreement with analogue profiles from Dabiri *et al.* (2007).

3.1. *Discussion*

According to the C_N reported in table 2, all cases should be classified as *cavitating*. On the other hand, the simulations, and especially those with $u_{in} = 0.07$ or lower, show no bubble formation, based on visual inspection of the density profiles.

This is not totally surprising, as it is well-known that cavitation presents several thresholds of both inception and detectability (Koivula 2000) and that a given C_N does

https://doi.org/10.1017/jfm.2013.271 Published online by Cambridge University Press

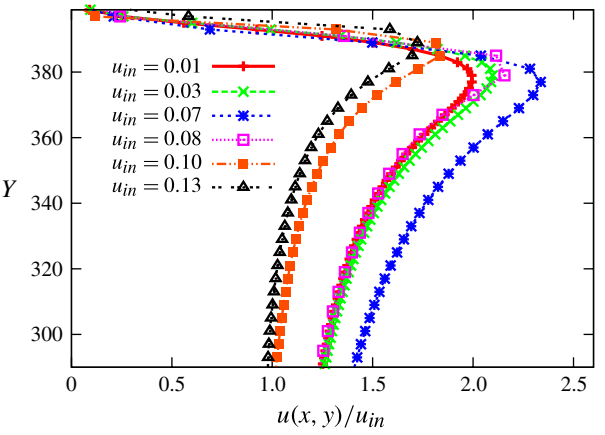


FIGURE 4. (Colour online) Close-up of the of normalized streamwise velocity in the inlet section of the nozzle channel, located at $x = 500$. The data are obtained for $h = 400$ and $G_1 = -15$ and $G_2 = 10.0$. The figure shows that the normalized velocity is smaller for $u_{in} = 0.10$ and $u_{in} = 0.13$, than for smaller inlet velocities, an effect that we ascribe to increasing dissipation.

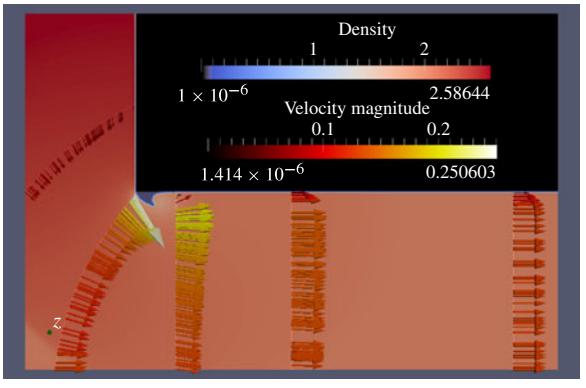


FIGURE 5. (Colour online) Velocity vector profiles in different cross-sections of nozzle channel at $Re \sim 2000$ and $t \sim 500$.

not uniquely identify the bubble configuration inside the flow (Brennen 1995; Joseph 1998; Dabiri *et al.* 2007).

An apparently more robust thermodynamic criterion to identify the actual cavitating conditions inside the flow, was proposed by Joseph (1998) and Dabiri *et al.* (2007), and usually referred to as the *minimum tension criterion*. The idea is as follows.

The pressure tensor T_{ab}, $a, b = x, y, z$, of a non-Newtonian fluid is given by $T_{ab} = -P\delta_{ab} + \tau_{ab}$, where P is the local pressure and τ_{ab} is the shear-stress tensor, obeying the incompressibility condition $\tau_{xx} + \tau_{yy} = 0$, and $\tau_{xy} = \tau_{yx}$.

Upon diagonalization, the pressure tensor delivers two diagonal components, T_{11} and T_{22}.

https://doi.org/10.1017/jfm.2013.271 Published online by Cambridge University Press

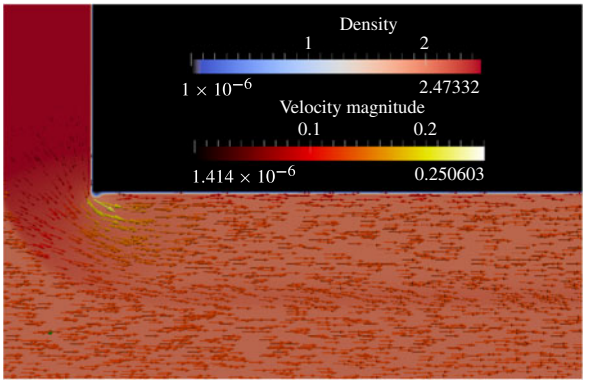


FIGURE 6. (Colour online) Density contours and vectors of velocity magnitude for $u_{in} = 0.13$ and $h = 400$, after $t \sim 150$ time steps. A cavitation bubble near the leading corner (shown in blue online) is visible.

u_{in}	P_{loc}	$\tau_{xx} \times 10^3$	$\tau_{yy} \times 10^3$	$\tau_{xy} \times 10^3$	T_{11}	T_{22}
0.01	0.046	−0.10	0.19	−0.033	−0.0458	−0.0461
0.03	0.046	−0.75	0.85	−0.160	−0.0452	−0.0468
0.07	0.031	−2.70	2.70	−0.333	−0.0283	−0.0337
0.08	0.030	−3.40	3.40	−0.633	−0.0265	−0.0355
0.10	0.039	−4.30	4.30	−1.250	−0.0345	−0.0435
0.13	0.040	−7.40	7.40	−3.000	−0.0320	−0.0480

TABLE 3. Stress components for the cases in table 2.

The minimum tension criterion proposed in Joseph (1998) and Dabiri *et al.* (2007) maintains that cavitation inception takes place under the condition

$$T_{11} + P_t > 0, \tag{3.2}$$

where P_t is a critical pressure threshold, approximately related to, but not necessarily coincident with, the local vapour pressure P_v or the critical pressure P_c (Joseph 1998; Dabiri *et al.* 2007).

Following Brennen (1995), it is known that the growth of a nucleus to a finite, observable size requires a finite residency time, under the conditions $P < P_v - \Delta P_c$, where ΔP_c is a proper pressure correction, which can be related to the surface tension, σ, of the fluid.

In our simulations, it was found that the minimum radius allowing the bubble to grow without being re-absorbed within the liquid phase is $R_b \sim 4$ lattice units (see figure 6).

With the surface tension value given in table 1, we find

$$\Delta P_c = \frac{\sigma}{R} \sim 0.0206. \tag{3.3}$$

As a result, we set $P_t = P_v - \Delta P_c = 0.062 - 0.0206 = 0.0414$.

https://doi.org/10.1017/jfm.2013.271 Published online by Cambridge University Press

It should be noted that, at Boltzmann's kinetic level, the shear is carried by the non-equilibrium component of the kinetic distribution function and, consequently, it does not affect the EOS, which only depends on equilibrium properties. As a result, from the kinetic perspective, Joseph's criterion amounts to stating that cavitation depends also on the non-equilibrium properties, which appears to be a very reasonable assumption.

We wish to emphasize that, since we simulate directly the kinetic equation, we do not have to make any assumption on the validity of this criterion, but simply verify *ex post* whether or not it is supported by the underlying kinetic physics.

By applying this Joseph–Brennen criterion, we find an excellent match with visual evidence, namely all cases with $u_{in} \geqslant 0.07$ satisfy Joseph's inequality (3.2), $T_{11} + P_c > 0$. This lends further support to Joseph's intuition that cavitation is very sensitive to local stress conditions.

In addition to concurring to the criteria for incipient cavitation, surface tension also affects the subsequent evolution of the bubble and, most notably, its dynamic morphology.

In figure 7, we report the density profiles for the case $h = 400$ and $u_{in} = 0.13$, by varying the repulsive strength $G_2 = 5, 10$ at a given value $G = G_1 + G_2 = -5$, so as to achieve the same EOS, but a smaller surface tension (from $\sigma = 0.0565$ to about $\sigma = 0.0412$, corresponding to, respectively, $16.3 \leqslant We \leqslant 22.2$).

The effects on the dynamic morphology of the cavitation bubble are dramatic: the cavitating bubble experiences a large deformation, which subsequently develops a thin filament, finally leading to breakup of the droplet.

4. Conclusions

Summarizing, we have presented what we believe is the first direct numerical evidence of flow-induced incipient cavitation, where cavitation bubbles emerge spontaneously as a result of the underlying non-ideal interactions, with no need for modelling criteria based on the fluid variables, such as pressure, velocity or stress. The simulations show that the onset of incipient cavitation is well-captured by a proper extension of Joseph's criterion based on minimum tension, as corrected with a surface-tension term. On the other hand, traditional criteria based on the cavitation number alone fail to predict incipient cavitation, as revealed by visual inspection of the flow configuration. Finally, the simulations also highlight a strong sensitivity of the bubble morphology to the surface tension. To convey a flavour of the computational cost, a typical LB simulation on a 1000^2 lattice, spanning 10^4 time steps, requires a few CPU hours on a standard laptop.

Appendix. LB for non-ideal fluids: the *two-belt* approach

The equilibrium distribution function is calculated in order to make the collision operator conserve mass and momentum: a common choice that satisfies the above constraints is the following

$$f_i^{eq} = w_i \rho \left(1 + \frac{1}{c_s^2} \boldsymbol{c}_i \cdot \boldsymbol{u} + \frac{1}{2c_s^4} (\boldsymbol{c}_i \cdot \boldsymbol{u})^2 - \frac{1}{2c_s^2} u^2 \right). \tag{A 1}$$

The main advantages of the LB method are twofold. First, from an applied point of view, this method is fully local. The dynamics takes place within a few neighbouring lattice nodes, allowing an efficient parallelization therefore the possibility to study complex flows at microscales with realistic physical models. Moreover, being

https://doi.org/10.1017/jfm.2013.271 Published online by Cambridge University Press

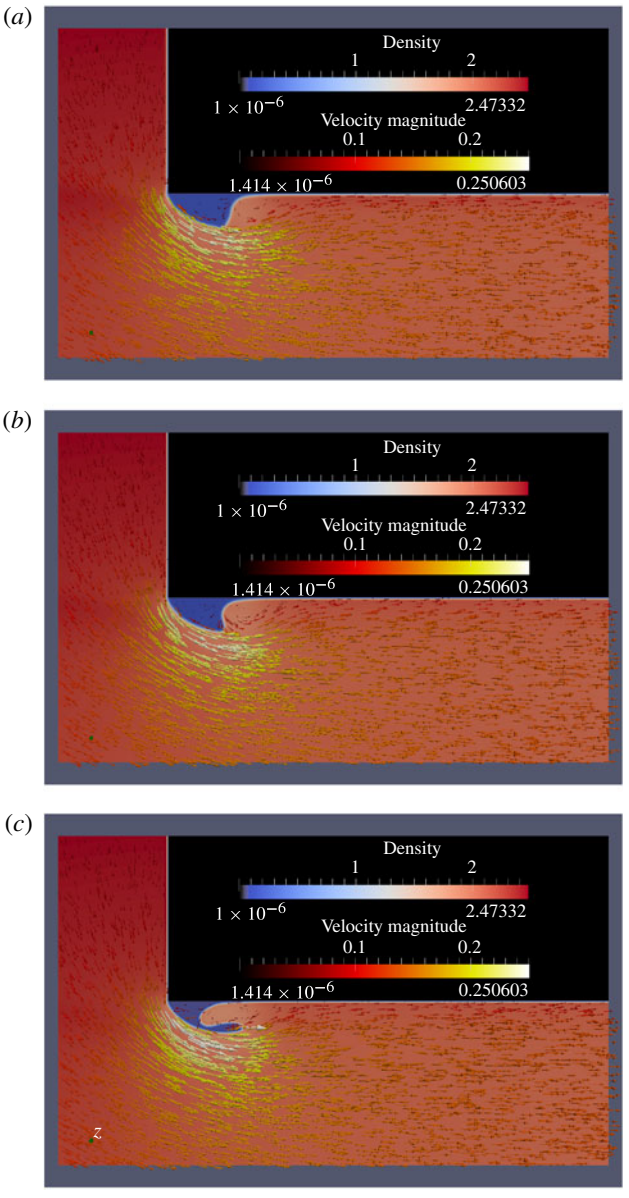


FIGURE 7. (Colour online) Density contours and vectors of velocity magnitude for $u_{in} = 0.13$ and $h = 400$, corresponding to $Re = 624$: (*a*) $G_1 = -5.0, G_2 = 0.0$, $We = 15.5$; (*b*) $G_1 = -10.0$ $G_2 = 5.0$ and $We = 18.2$; (*c*) $G_1 = -15.0$, $G_2 = 10.0$ and $We = 22.2$. The surface tension values are reported in table 1. All snapshots are obtained after $\sim$1000 time steps.

a diffuse-interface method, there is no need to 'define' the interface position, the interface physics arising naturally from the microscopic interactions between the lattice populations. Such advantage is key, because most of the numerical limitations in studying multiphase flows are due to the difficulties in tracking the interface.

https://doi.org/10.1017/jfm.2013.271 Published online by Cambridge University Press

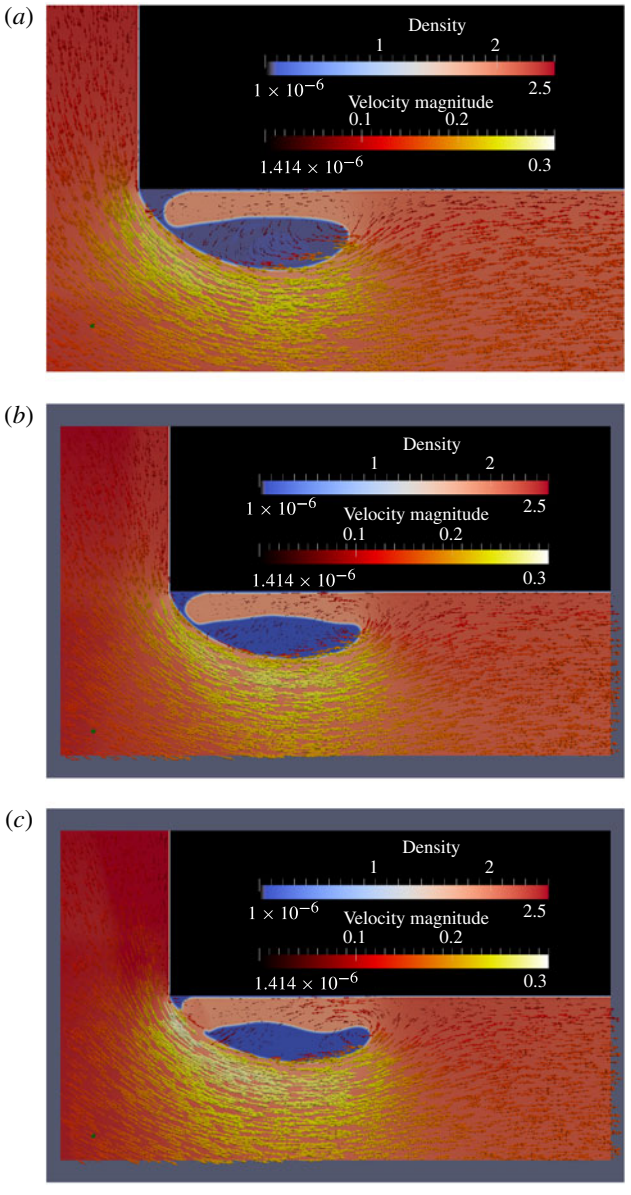


FIGURE 8. (Colour online) Rupture of the cavitation bubble at $\sigma = 0.0412$, corresponding to $We = 22.2$. The main parameters are $u_{in} = 0.13$, $h = 400$, $G_1 = -15.0$ and $G_2 = 10$. The snapshots are taken after ∼2000 time steps.

A.1. *Two-belt EOS*

In the two-belt EOS, the pseudo-potential force consists of two separate components (Falcucci *et al.* 2010*b*, 2011), $\boldsymbol{F}(\boldsymbol{x}, t) = \boldsymbol{F}_1(\boldsymbol{x}, t) + \boldsymbol{F}_2(\boldsymbol{r}, t)$, defined as follows:

$$\boldsymbol{F}_1(\boldsymbol{x}, t) = G_1 \psi(\boldsymbol{x}; t) \sum_{i=0}^{b_1} w_i \psi(\boldsymbol{x}_{1i}, t) \boldsymbol{c}_{1i} \Delta t \tag{A 2}$$

https://doi.org/10.1017/jfm.2013.271 Published online by Cambridge University Press

$$\boldsymbol{F}_2(\boldsymbol{x}, t) = G_2\psi(\boldsymbol{x}; t)\sum_{i=0}^{b_1} p_{1i}\psi(\boldsymbol{x}_{1i}, t)\boldsymbol{c}_{2i}\Delta t + G_2\psi(\boldsymbol{x}; t)\sum_{i=0}^{b_2} p_{2i}\psi(\boldsymbol{x}_{2i}, t)\boldsymbol{c}_{2i}\Delta t \quad (A\,3)$$

where the local pseudo-potential governing the interaction is given by $\psi = \sqrt{\rho_0}(1 - e^{-\rho/\rho_0})$.

In (A 2) and (A 3), the indices $k = 1, 2$ refer to the first and second Brillouin zones in the lattice (belts), and $\boldsymbol{c}_{ki}$, p_{ki} are the corresponding discrete speeds and associated weights; $\boldsymbol{x}_{ki} \equiv \boldsymbol{x} + \boldsymbol{c}_{ki}\Delta t$ are the displacements along the ith direction in the kth belt.

The first belt is discretized with 9 speeds ($b_1 = 8$), while the second belt is discretized with 16 speeds ($b_2 = 16$) and the weights are chosen in such a way as to fulfil the following relations (Falcucci *et al.* 2008): $\sum_{i=0}^{b_1} w_i = \sum_{i=0}^{b_1} p_{i1} + \sum_{i=0}^{b_2} p_{i2} = 1$; $\sum_{i=0}^{b_1} w_i c_i^2 = \sum_{i=0}^{b_1} p_{i1} c_{i1}^2 + \sum_{i=0}^{b_2} p_{i1} c_{i2}^2 = c_s^2$, $c_s^2 = 1/3$ being the lattice sound speed.

Taylor expansion of (A 2), (A 3) to second order delivers the following non-ideal EOS $p \equiv P/c_s^2 = \rho + ((G_1 + G_2)/2)c_s^2\ \psi^2(\boldsymbol{x}, t)$. Further expansion to fourth–order provides the following expressions for the surface tension

$$\gamma = -\frac{(G_1 + \xi G_2)}{2} c_s^4 \int_{\infty}^{\infty} |\partial_y \psi|^2 \, \mathrm{d}y \quad (A\,4)$$

where y runs across the phase interface. Note that the double potential allows us to change the EOS and the surface tension independently. In particular, since $\xi = 12/7 > 1$ the effect of the repulsive belt is to lower the surface tension at a given value of $G_1 + G_2$.

The main appeal of LB for computational studies of cavitation is its extreme simplicity and ensuing computational efficiency. The liquid–vapour interface emerges spontaneously from the thermodynamic properties of the fluid, namely its non-ideal equations state and surface tension, with no need to imposing any *ad hoc* criteria to locate it, based on the space–time distribution of the fluid pressure or other hydrodynamic quantities.

REFERENCES

BENZI, R., SUCCI, S. & VERGASSOLA, M. 1992 The lattice Boltzmann equation: theory and applications. *Phys. Rep.* **222** (3), 145–197.

BREMOND, N., ARORA, M., OHL, C.-D. & LOHSE, D. 2005 Cavitation on surfaces. *J. Phys.: Condens. Matter* **17**, S3603.

BRENNEN, C. 1995 *Cavitation and Bubble Dynamics*. Oxford University Press.

BRUJAN, E., IKEDA, T. & MATSUMOTO, Y. 2012 Shock wave emission from a cloud of bubbles. *Soft Matt.* **8**, 5777–5783.

CHEN, X.-P., ZHONG, C.-W. & YUAN, X.-L. 2011 Lattice Boltzmann simulation of cavitating bubble growth with large density ratio. *Comput. Maths Applics.* **61** (12), 3577–3584.

COLOSQUI, C., FALCUCCI, G., UBERTINI, S. & SUCCI, S. 2012 Mesoscopic simulation of non-ideal fluids with self-tuning of the equation of state. *Soft Matt.* **8**, 3798–3809.

DABIRI, S., SIRIGNANO, W. & JOSEPH, D. 2007 Cavitation in an orifice flow. *Phys. Fluids* **19**, 072112.

DARBANDI, M. & SADEGHI, H. 2010 Numerical simulation of orifice cavitating flows using two-fluid and three-fluid cavitation models. *Numer. Heat Transfer* A **58**, 505–526.

EPSTEIN, P. & PLESSET, M. 1950 On the stability of gas bubbles in liquid gas solutions. *J. Chem. Phys.* **18**, 1505–1509.

FALCUCCI, G., BELLA, G., CHIATTI, G., CHIBBARO, S., SBRAGAGLIA, M. & SUCCI, S. 2007 Lattice Boltzmann models with mid-range interactions. *Commun. Comput. Phys.* **2** (6), 1071–1084.

https://doi.org/10.1017/jfm.2013.271 Published online by Cambridge University Press

FALCUCCI, G., BELLA, G., UBERTINI, S., PALPACELLI, S. & DE MAIO, A. 2010*a* Lattice Boltzmann modeling of Diesel spray formation and break-up. *SAE Intl J. Fuels Lubr.* **3**, 582–593.

FALCUCCI, G., CHIBBARO, S., SUCCI, S., SHAN, X. & CHEN, H. 2008 Lattice Boltzmann spray-like fluids. *Europhys. Lett.* **82**, 24005.

FALCUCCI, G., UBERTINI, S., BELLA, G. & SUCCI, S. 2013 Lattice boltzmann simulation of cavitating flows. *Commun. Comput. Phys.* **13**, 685–695.

FALCUCCI, G., UBERTINI, S., BISCARINI, C., DI FRANCESCO, S., CHIAPPINI, D., PALPACELLI, S., DE MAIO, A. & SUCCI, S. 2011 Lattice Boltzmann methods for multiphase flow simulations across scales. *Commun. Comput. Phys.* **9** (2), 269–296.

FALCUCCI, G., UBERTINI, S. & SUCCI, S. 2010*b* Lattice Boltzmann simulations of phase-separating flows at large density ratios: the case of doubly-attractive pseudo-potentials. *Soft Matt.* **6**, 4357–4365.

FRANC, J.-P. & MICHEL, J.-M. (Eds) 2005 *Fundamentals of Cavitation*. Kluwer Academic.

GAVAISES, M., PAPOULIAS, D., ANDRIOTIS, A. & GIANNADAKIS, E. 2007 Link between cavitation development and erosion damage in diesel injector nozzles. *SAE Tech. Paper* 2007-01-0246.

GIANNADAKIS, E., GAVAISES, M. & ARCOUMANIS, C. 2008 Modelling of cavitation in diesel injector nozzles. *J. Fluid Mech.* **616**, 153–193.

GIANNADAKIS, E., PAPOULIAS, D., GAVAISES, M., ARCOUMANIS, C., SOTIERIOU, C. & TANG, W. 2007 Evaluation of the predictive capability of Diesel nozzle cavitation models. *SAE Tech. Paper* 2007-01-0245.

HILGENFELDT, A., BRENNER, M. P., GROSSMANN, S. & LOHSE, D. 1998 Analysis of the Rayleigh–Plesset dynamics for sonoluminescing bubbles. *J. Fluid Mech.* **365**, 171–204.

JOSEPH, D. 1998 Cavitation and the state of stress in a flowing liquid. *J. Fluid Mech.* **366**, 367–378.

KOIVULA, T. 2000 On cavitation in fluid power. In *Proceedings of the 1st FPNI-PhD Symp. Hamburg 2000*, pp. 371–382.

KUMAR, P. & SAINI, R. P. 2010 Study of cavitation in hydro turbines – a review. *Renewable and Sustainable Energy Reviews* **14** (1), 374–383.

LEE, W. & REITZ, R. 2009 Simulation of transient cavitation processes in diesel injectors using kiva with a homogeneous equilibrium model. In *Proceedings of the International Multidimensional Engine Modeling User's Group Meeting, Detroit (MI)*.

LOHSE, D. 2005 Cavitation hots up. *Nature* **434**, 33–34.

OHL, C.-D., ARORA, M., IKINK, R., DE JONG, N., VERSLUIS, M., DELIUS, M. & LOHSE, D. 2006 Sonoporation from jetting cavitation bubbles. *Biophys. J.* **91**, 4285–4295.

PAYRI, F., PAYRI, R., SALVADOR, F. & MARTINEZ-LOPEZ, J. 2012 A contribution to the understanding of cavitation effects in Diesel injector nozzles through a combined experimental and computational investigation. *Comput. Fluids* **58**, 88–101.

PECHA, R. & GOMPF, B. 2000 Microimplosions: cavitation collapse and shock wave emission on a nanosecond time scale. *Phys. Rev. Lett.* **84**, 1328–1332.

PLESSET, M. S. & PROSPERETTI, A. 1977 Bubble dynamics and cavitation. *Annu. Rev. Fluid Mech.* **9**, 145–185.

SBRAGAGLIA, M., BENZI, R., BIFERALE, L., SUCCI, S., SUGIYAMA, K. & TOSCHI, F. 2007 Generalized lattice Boltzmann method with multi-range pseudo-potential. *Phys. Rev.* E **75**, 026702.

SHAN, X. & CHEN, H. 1993 Lattice Boltzmann model for simulating flows with multiple phases and components. *Phys. Rev.* E **47**, 1815–1820.

SHAN, X. & CHEN, H. 1994 Simulation of nonideal gases and liquid–gas phase transitions by the lattice Boltzmann equation. *Phys. Rev.* E **49**, 2941–2948.

SUCCI, S. 2001 *The Lattice Boltzmann Equation for Fluid Dynamics and Beyond*. Clarendon.

SUKOP, M. C. & OR, D. 2005 Lattice Boltzmann method for homogeneous and heterogeneous cavitation. *Phys. Rev.* E **71**, 046703.

https://doi.org/10.1017/jfm.2013.271 Published online by Cambridge University Press

ZALESKI, S., LI, J. & SUCCI, S. 1995 Two-dimensional Navier–Stokes simulation of deformation and breakup of liquid patches. *Phys. Rev. Lett.* **75**, 244–247.

ZHONG, M., ZHONG, C. & BAI, C. 2012 A high-order discrete scheme of Lattice Boltzmann method for cavitation simulation. *Adv. Comput. Sci. Appls* **1**, 73–77.

ZWAAN, E., LE GAC, S., TSUJI, K. & OHL, C.-D. 2007 Controlled cavitation in microfluidic systems. *Phys. Rev. Lett.* **98**, 254501.

https://doi.org/10.1017/jfm.2013.271 Published online by Cambridge University Press